The aerodynamic wall

Caroline Cohen[1], Baptiste Darbois-Texier[1], Guillaume Dupeux[2], Eric Brunel[3], David Quéré[1] and Christophe Clanet[2]

[1]LadHyX, UMR 7646 du CNRS, Ecole Polytechnique, 91128 Palaiseau Cedex, France
[2]PMMH, UMR 7636 du CNRS, ESPCI, 75005 Paris, France
[3]DCSD, ONERA, 59000 Lille, France

We study the trajectory of dense projectiles subjected to gravity and drag at large Reynolds number. We show that two types of trajectories can be observed: if the initial velocity is smaller than the terminal velocity of free fall, we observe the classical Galilean parabola: if it is larger, the projectile decelerates with an asymmetric trajectory first drawn by Tartaglia, which ends with a nearly vertical fall, as if a wall impeded the movement. This regime is often observed in sports, fireworks, watering, etc. and we study its main characteristics.

1. Introduction

Particles moving in air usually exhibit a curved trajectory with a strong asymmetry with respect to the maximum. Three examples are presented in figure 1, which illustrate (*a*) grinding, (*b*) fireworks and (*c*) field watering. This asymmetry historically led to the singular limit of 'triangular' trajectories reported in studies of artillery and illustrated in figure 2. According to Tartaglia [1,4], the trajectory was composed of two main phases, a straight violent motion at the exit of the canon (segment AB in figure 2*a*) and a final vertical path called natural (segment EF). The two limits were connected via a circular path.

Owing to its application in the military context [5] and more recently in sports [6], this ballistic problem has also been studied in detail and geometrical constructions [7], numerical solutions [8] and theoretical discussions [9,10] have been proposed to account for the trajectory. One of the more famous works on the subject is probably the 'dialogues concerning the two new sciences' [2] first published in 1638, one century after Tartaglia. The fourth and last day of the dialogues is dedicated to the motion of projectiles. For the first

Figure 1. Examples of asymmetric particles trajectories: (*a*) grinding (extracted from http://www.eartaker.net/machining/grinding/images/sparks.jpg), (*b*) fireworks (extracted from the free image section of Flickr), (*c*) water jet (© Gaby Kooijman, http://www.dreamstime.com). (Online version in colour.)
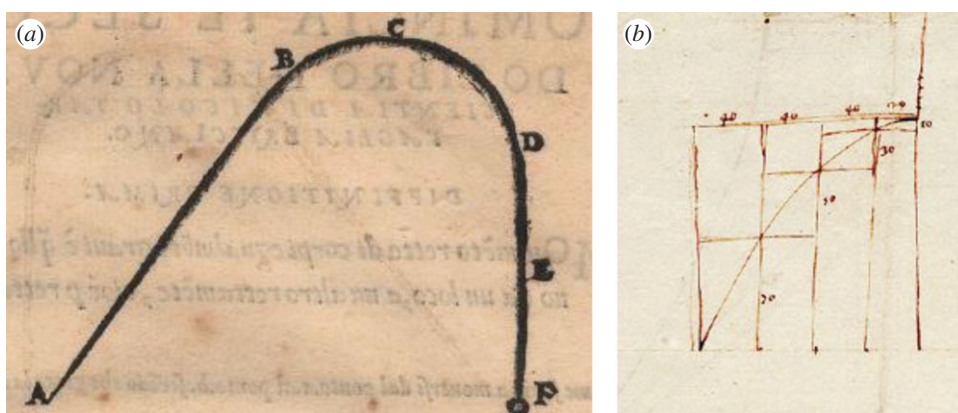

Figure 2. Historical illustrations of the two asymptotic trajectories expected in ballistics: (*a*) Tartaglia's discussion of a bullet path extracted from his treatise *Nova Scientia* first published in 1537 [1]. (*b*) Galileo's original construction of the parabolic path. This drawing is discussed in the theorem 1 of the fourth day of the two new sciences first published in 1638 [2]. Complementary information can be found in [3]. (Online version in colour.)

time, it describes the parabolic trajectory, an example of which is reproduced in figure 2*b*. Contrary to the Tartaglia curve which has well-defined asymptotes, the parabola does not have any.

Here, we study experimentally and theoretically the ballistic problem and show that, depending on the initial velocity, the two types of trajectories can be observed.

2. A brief overview of external ballistics

While the internal ballistics focuses on the physics of launching (inside the bore of the cannon), the general topic of external ballistics is to determine the trajectory of a projectile while moving in air [5,9]. For a particle of mass M and velocity $\boldsymbol{U}$, the whole problem is to solve the equation of motion:

$$M\frac{\mathrm{d}\boldsymbol{U}}{\mathrm{d}t} = \boldsymbol{F}_G + \boldsymbol{F}_A, \tag{2.1}$$

where $\boldsymbol{F}_G = M\boldsymbol{g}$ is the weight and $\boldsymbol{F}_A$ the aerodynamic force. This equation must be solved with the initial condition $\boldsymbol{U}(t=0) = \boldsymbol{U}_0$. In the plane $(\boldsymbol{U}_0, \boldsymbol{g})$, this problem can be discussed with the conventions presented in figure 3. Apart from the actual shape $y(x)$, the points of interest for the applications are usually the range x_0, the maximal height h and the optimal launching angle $\theta^\star$ which maximizes the range.
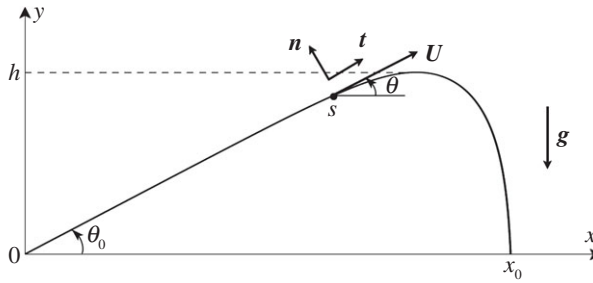
Figure 3. Presentation of the problem and conventions.

Without air ($F_A = 0$), the solution is the classical parabola, first found by Galileo [2], for which $\theta^\star = \pi/4$, $h = U_0^2/2g \sin^2 \theta_0$ and $x_0 = U_0^2/g \sin 2\theta_0$, where θ_0 is the launching angle. With air, equation (2.1) is not closed in the sense that the aerodynamic force depends on the velocity $F_A(U)$.

To illustrate the diversity of the ballistic problem in this limit, we briefly discuss the relations $F_A(U)$ obtained with spheres. In this discussion, we use the classical drag–lift decomposition of the aerodynamical force $F_A = F_D + F_L$, where F_D stands for the drag, that is the part of the force aligned with the velocity and F_L the part which is perpendicular to it.

For incompressible Newtonian fluids (density ρ, viscosity η), the motion of non-spinning spheres (radius R, velocity U) in an infinite domain has early become a classical subject [11]. In the low Reynolds number limit ($Re \equiv \rho U 2R/\eta \ll 1$ with $U = |U|$), Stokes [12] has established theoretically that the drag force experienced by the sphere during its motion is $F_D = -6\pi \eta U R$. Experimentally, this result has been verified by several authors in the range $Re \leq 1$ [13,14]. In the high Reynolds number domain, besides the classical d'Alembert paradox [15], Newton [16] is probably the first to propose an heuristic expression for the drag: $F_D = -1/2\rho C_D \pi R^2 U U$. According to the early experiments performed by Eiffel [17], $C_D \approx 0.4 - 0.5$. This value has since been confirmed by several authors for the range: $10^3 < Re < 2.10^5$. In the intermediate range, the asymptotic expansion method proposed by Oseen [18] has led to many theoretical developments [19]. The drag crisis experienced by the sphere once the boundary layer becomes turbulent (around $Re \approx 3.10^5$) has also been deeply studied [20–22].

For spinning spheres, according to Barkla [23], the work seems to go back to Robins [24] and then Magnus [25], who is credited for the associated lift force. Besides these academic studies, the widespread use of balls in sports has also motivated many studies, in baseball [26] and golf [27] in particular, a review of which can be found in reference [6]. These studies show that the sphere experiences a lift force $F_L = 1/2\rho C_R \pi R^3 \omega_0 \wedge U$, where ω_0 is the spin vector and C_R a coefficient which can depend on the Reynolds number, the Spin number ($Sp = R\omega_0/U$) and surface roughness [28]. For sports balls, the dependency of C_R with Re and Sp is modest [29]. In baseball for example, Nathan concludes that in the range of spin number between 0.1 and 0.6 and Reynolds number between 1.1×10^5 and 2.4×10^5, the coefficient C_R remains almost constant and equal to 0.5 ± 0.1 [26].

What we retain from this discussion is that the expression of the aerodynamical force $F_A(U)$ depends on both the Reynolds number and spin. In this study, we first focus on the large Reynolds number pure drag limit where the equation of motion for a dense particle takes the form:

$$M\frac{dU}{dt} = Mg - \frac{1}{2}\rho C_D \pi R^2 U U. \tag{2.2}$$

In the steady state ($dU/dt = 0$), the velocity is equal to the terminal velocity $U = -U_\infty e_y$ with $U_\infty = \sqrt{2Mg/\pi R^2 \rho C_D}$.

3. Experimental results

(a) Measurement of the terminal velocity U_∞

The projectiles we use are sport balls. To measure their terminal velocity, U_∞, we conducted experiments in the vertical wind tunnel SV4 of ONERA (the French Aerospace Laboratory) in Lille. This unique facility blows air at 20°C up to $50\,\mathrm{m\,s^{-1}}$ in a $4\,\mathrm{m}$ cylindrical vein [30]. The protocol consists of increasing the velocity step by step up to levitation. At each step, we wait 1 min for the flow to stabilize in the vein. The particle is then introduced in the centre part of the channel. If it falls, we keep increasing the velocity up to the point where it starts to levitate. When this levitation state is reached, we measure the velocity with a VT 200 Kimo anemometer and a pitot tube. Two examples of levitation are presented in figure 4, one for a Jabulani soccer ball leading to $U_\infty = 30\,\mathrm{m\,s^{-1}}$ (a) and the other for a feather shuttlecock leading to $U_\infty = 6.7\,\mathrm{m\,s^{-1}}$ (b). All the results are presented in table 1. For each projectile (first column), we measure its diameter ($2R$ in second column), its mass (M in third column) and the terminal velocity (U_∞ in fourth column). The corresponding Reynolds number $Re_\infty = 2RU_\infty/\nu$ and drag coefficient $C_D = 2Mg/(\rho U_\infty^2 \pi R^2)$ are calculated in columns 5 and 6 using for the density and viscosity, the tabulated values at 20° [31]: $\rho = 1.20\,\mathrm{kg\,m^{-3}}$ and $\nu = \eta/\rho = 15.10^{-6}\,\mathrm{m^2\,s^{-1}}$. We observe in these columns that the Reynolds number is of the order of 10^5 and that the drag coefficient takes values between 0.1 and 0.6. Focusing on spherical particles, we note that their drag coefficient for Reynolds numbers smaller than 10^5 take values close to the classical 0.45, whereas their values decrease to approximately 0.2 for Reynolds numbers larger than 10^5. This behaviour is consistent with the behaviour of the drag coefficient in the region of the drag crisis [6,32].

The last two columns in table 1 respectively indicate the fastest hit recorded on fields, U_{max}, and the ratio between this maximal velocity of the game and the terminal velocity of the ball. We observe in this last column that the record velocity is larger than the terminal velocity except for handball and basketball.

(b) Qualitative observations

For the two extreme sports reported in table 1, namely basketball and badminton, we present in figure 5 two chronophotographies showing the trajectories of the particles obtained respectively, with $U_0/U_\infty = 0.48$ (a) and $U_0/U_\infty = 8.9$ (b). The trajectory of the basketball presents a left–right symmetry with respect to the maximum, with a continuous evolution of the velocity. For the badminton shuttlecock, the symmetry is broken, and the velocity first decreases from the hit location, and then reaches an almost constant value. The evolution of the trajectory with the hit velocity and initial angle are discussed in the §2c.

(c) Trajectories

Among the different sports projectiles that we have characterized in table 1 the shuttlecock is the one which enables (owing to its low terminal velocity) to maximize the range of the ratio U_0/U_∞. We thus use it to study how this ratio affects the shape of the trajectory. The shuttlecock for these experiments is presented in figure 6a: it is a MAVIS 370, composed of a plastic skirt (S) fixed on a cork (C). The length of the skirt is $L = 60\,\mathrm{mm}$ and its radius $R = 34\,\mathrm{mm}$. The whole mass is $M = 5.3\,\mathrm{g}$, 3 g for the cork and 2.3 g for the skirt. Using a Deltalab EA600 wind tunnel, we have measured the drag of shuttlecocks free to rotate. The evolution of the drag coefficient with the Reynolds number is presented in figure 6b. We observe that $C_D \approx 0.65 \pm 7\%$, independent of the Reynolds number. This value is consistent with the one measured in the vertical wind tunnel and reported in table 1 [33].

Concerning the trajectory, we present in figure 7 several experiments (circles) obtained with different initial velocities U_0 and inclination angle θ_0. The timestep between two data points is 100 ms. We observe that the asymmetry increases with both the hit velocity and initial angle.

5

rspa.royalsocietypublishing.org Proc. R. Soc. A **470**: 20130497

Figure 4. Terminal velocity measurements performed in the vertical wind tunnel SV4 of ONERA-Lille: (a) levitating Jabulani soccer ball at $U_\infty = 30$ m s^{-1}; (b) levitating feather shuttlecock at $U_\infty = 6.7$ m s^{-1}. (Online version in colour.)

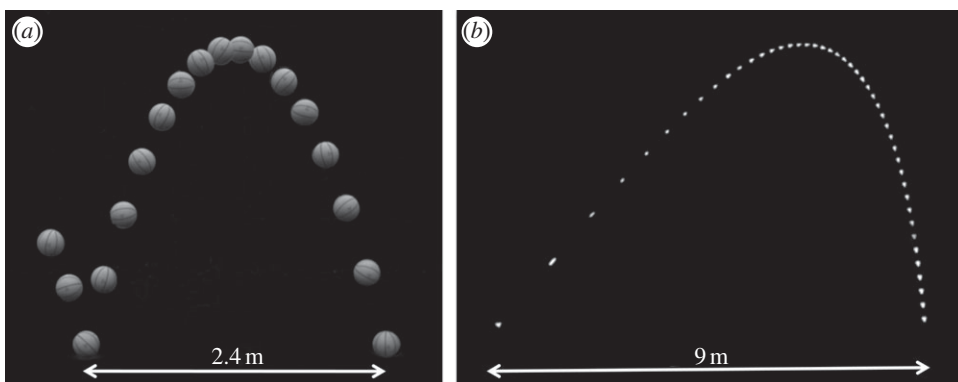**Figure 5.** Chronophotography of two sport particles: (a) basketball with $dt = 40$ ms, $\theta_0 = 74°$, $U_0 = 15$ m s^{-1}. (b) shuttlecock with $dt = 40$ ms, $\theta_0 = 60°$, $U_0 = 40$ m s^{-1}.

Table 1. Characteristics of various sports balls and projectiles: diameter ($2R$), mass (M), terminal velocity (U_∞), corresponding Reynolds number ($Re_\infty = 2RU_\infty/\nu$) and drag coefficient ($C_D = 2Mg/(\rho U_\infty^2 \pi R^2)$). The last two columns present the fastest hit (U_{max}) and its ratio with the terminal velocity (U_{max}/U_∞).

sport	2R (cm)	M (g)	U_∞ (m s^{-1})	Re_∞ ×10^5	C_D	U_{max} (m s^{-1})	U_{max}/U_∞
badminton	6.0	5	6.7	0.27	0.60	117	17.5
table tennis	4.0	2.5	9.5	0.25	0.36	32	3.4
tennis	6.5	55	22	0.95	0.55	73	3.3
golf	4.2	45	48	1.34	0.26	91	1.9
baseball	7.0	145	40	1.86	0.38	55	1.4
soccer ball	21	480	30	4.2	0.25	51	1.7
volleyball	21	210	20	4.5	0.25	36	1.1
handball	19	450	36	4.6	0.2	28	0.75
basketball	24	650	31	4.96	0.24	22	0.7

6

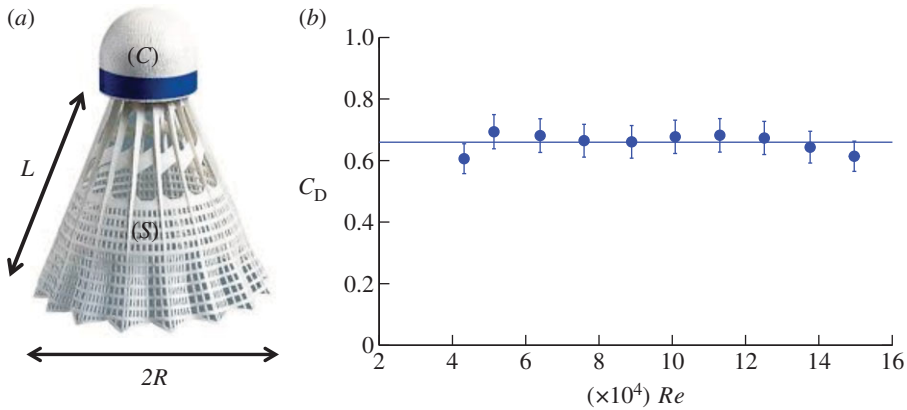rspa.royalsocietypublishing.org   *Proc. R. Soc. A* **470**: 20130497

Figure 6. (*a*) Geometrical characteristics of a shuttlecock. (*b*) Evolution of the drag coefficient, $C_D = 2F_D/\rho \pi R^2 U^2$, of a shuttlecock with the Reynolds number $Re = 2RU/\nu$. (Online version in colour.)
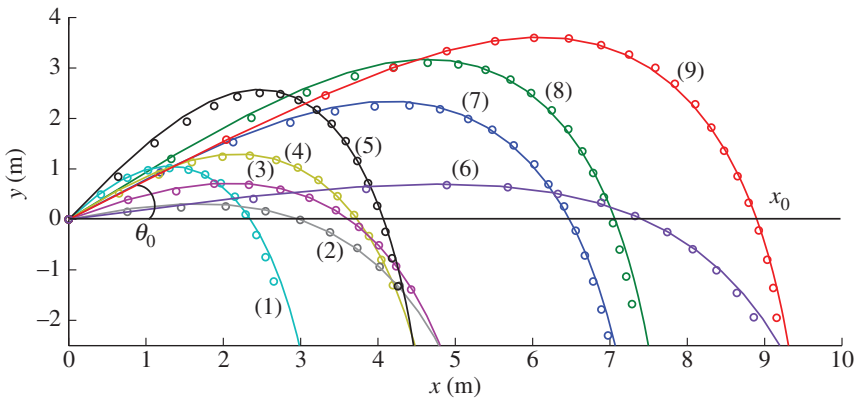

Figure 7. Comparison between the experimental trajectory (circles) and the trajectory calculated with the pure drag equation (2.2) (solid line) for different initial conditions: (1) $U_0 = 6.8\,\mathrm{m\,s^{-1}}, \theta_0 = 55°$, (2) $U_0 = 9.6\,\mathrm{m\,s^{-1}}, \theta_0 = 18°$, (3) $U_0 = 9.5\,\mathrm{m\,s^{-1}}, \theta_0 = 30°$, (4) $U_0 = 9.7\,\mathrm{m\,s^{-1}}, \theta_0 = 44°$, (5) $U_0 = 13.4\,\mathrm{m\,s^{-1}}, \theta_0 = 58°$, (6) $U_0 = 32.3\,\mathrm{m\,s^{-1}}, \theta_0 = 12°$, (7) $U_0 = 19.8\,\mathrm{m\,s^{-1}}, \theta_0 = 39°$, (8) $U_0 = 24.7\,\mathrm{m\,s^{-1}}, \theta_0 = 44°$ and (9) $U_0 = 37.6\,\mathrm{m\,s^{-1}}, \theta_0 = 38°$. (Online version in colour.)

More quantitatively, the numerical integrations of equation (2.2) are also presented with solid lines in figure 7. Without any adjustable parameter, the comparison with the experimental data is convincing for all initial conditions. We underline that in addition to their constant drag coefficient (figure 6*b*), shuttlecocks also present the advantage (compared with spheres) of having no additional Magnus lift.

(d) Saturation of the range

The range x_0 is defined in figures 3 and 7 as the location on the horizontal axis where the particle returns to its initial height [$y(x_0) = 0$]. As noted in figure 7, the range changes with both the initial angle and velocity. We report in figure 8*a*, the evolution of its reduced value $x_0/\mathcal{L}\cos\theta_0$ as a function of the reduced speed $(U_0/U_\infty)^2 \sin\theta_0$. The characteristic length $\mathcal{L}$ is linked to the terminal velocity via the relation $\mathcal{L} = U_\infty^2/g$. In the parabolic limit, one expects the linear relationship between the two quantities: $x_0/\mathcal{L}\cos\theta_0 = 2(U_0/U_\infty)^2 \sin\theta_0$. This linear dependency is presented with a dashed black line in figure 8*a*. It only fits the data obtained in the low velocity limit: $(U_0/U_\infty)^2 \sin\theta_0 \leq 1$. For larger velocities, the range strongly deviates from the gravitational limit
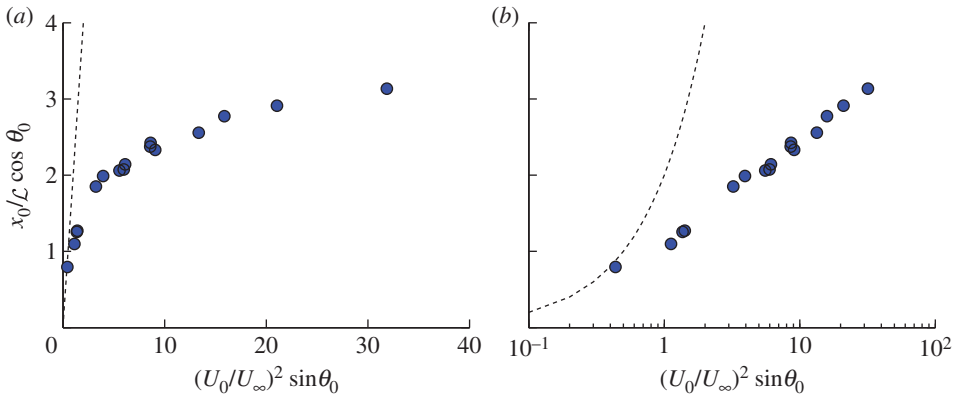
Figure 8. (*a*) Evolution of the reduced range $x_0/\mathcal{L} \cos\theta_0$ as a function of the reduced velocity $(U_0/U_\infty)^2 \sin\theta_0$. The experimental data are presented with dots. The black dashed line shows the low-velocity gravitational domain. (*b*) Same set of data presented in logline to emphasize the logarithmic saturation of the range. Again, the dashed line presents the parabolic prediction. (Online version in colour.)

and almost saturates: for instance, with $(U_0/U_\infty)^2 \sin\theta_0 = 30$, we measure $x_0/\mathcal{L} \cos\theta_0 = 3$ instead of 60. To characterize the saturation, we present in figure 8*b* the same set of data in a logline plot. This reveals the logarithmic saturation of the range: $x_0 \sim \mathcal{L} \cos\theta_0 \ln[(U_0/U_\infty)^2 \sin\theta_0]$.

4. Analysis of the trajectory

(a) Two exact solutions

The vertical launching limit ($\boldsymbol{U}_0 \wedge \boldsymbol{g} = 0$) can be solved analytically. If $\boldsymbol{U}_0$ is oriented downwards ($\boldsymbol{U}_0 = -U_0 \boldsymbol{e}_y$, $\theta_0 = -\pi/2$), equation (2.2) leads to: $(U/U_\infty)^2 = 1 + [(U_0/U_\infty)^2 - 1]e^{2y/\mathcal{L}}$. The velocity simply relaxes exponentially from its initial value $\boldsymbol{U}_0$ to its final value U_∞ over the characteristic length $\mathcal{L}$. When the initial velocity is positive, ($\boldsymbol{U}_0 = +U_0 \boldsymbol{e}_y$, $\theta_0 = +\pi/2$) the solution of equation (2.2) is $(U/U_\infty)^2 = -1 + [(U_0/U_\infty)^2 + 1]e^{-2y/\mathcal{L}}$. In this limit, the particle first decelerates and stops at the maximal height h, before falling downwards with the solution obtained for $\theta_0 = -\pi/2$ and $U_0 = 0$. The maximum height can be written as

$$h = \frac{\mathcal{L}}{2} \ln\left[1 + \left(\frac{U_0}{U_\infty}\right)^2\right]. \tag{4.1}$$

In the low velocity limit ($U_0/U_\infty \ll 1$), this equation reduces to the Galilean result, $h = U_0^2/2g$, with a quadratic dependency on the launching speed. However, in the large velocity limit ($U_0/U_\infty \gg 1$), this expression reveals that h mainly depends on its aerodynamic length $\mathcal{L}$ with a weak logarithmic dependency on the launching speed.

(b) Origin of the aerodynamical wall

We continue the analysis of equation (2.2) in the general case ($\boldsymbol{U}_0 \wedge \boldsymbol{g} \neq 0$) by discussing the origin of the aerodynamical wall: without drag ($C_D = 0$), equation (2.2) shows that the particle never reaches a steady state but always accelerates owing to gravity. With drag ($C_D \neq 0$), a steady state ($d\boldsymbol{U}/dt = 0$) appears in equation (2.2) where the velocity of the particle is

$$U_\infty \boldsymbol{U}_\infty = \mathcal{L}\boldsymbol{g}. \tag{4.2}$$

In this final stage (4.2), the velocity $\boldsymbol{U}_\infty$ is aligned with the gravitational acceleration $\boldsymbol{g}$ which means that the trajectory is vertical. As soon as the drag appears, there is thus a vertical asymptote

8

on the trajectory. This vertical asymptote is reached within the characteristic distance $\mathcal{L}$. This point can be shown by rewriting the equation of motion in the form:

$$U\frac{\mathrm{d}\boldsymbol{U}}{\mathrm{d}s} = \frac{1}{\mathcal{L}}(U_\infty \boldsymbol{U}_\infty - U\boldsymbol{U}), \tag{4.3}$$

where s is the arc length along the trajectory. The projection of this equation along the $\boldsymbol{e}_x$ direction leads to $\mathrm{d}U_x/\mathrm{d}s = -U_x/\mathcal{L}$, where U_x is the horizontal component of the velocity. This equation can be integrated with the initial condition where $U_{x0} = U_x(s=0) = U_0\cos(\theta_0)$ and we find

$$U_x(s) = U_{x0}\exp(-s/\mathcal{L}). \tag{4.4}$$

If $U_{x0} \neq 0$, this equation states that the horizontal component of the velocity vanishes exponentially within the distance $\mathcal{L}$. Beyond this distance, $\boldsymbol{U}$ and $\boldsymbol{U}_\infty$ are expected to be aligned. The distance $\mathcal{L}$ is thus expected to characterize the location of the aerodynamical wall. This point is further discussed in §4d.

(c) Two different regimes

To identify the parameters which govern the whole trajectory, we use the reduced variables $\bar{U} = U/U_0$ and $\bar{s} = s/\mathcal{L}$. The above equation of motion (4.3) becomes

$$\bar{U}\frac{\mathrm{d}\bar{\boldsymbol{U}}}{\mathrm{d}\bar{s}} = -\left(\frac{U_\infty}{U_0}\right)^2 \boldsymbol{e}_y - \bar{U}\bar{\boldsymbol{U}}. \tag{4.5}$$

Equation (4.5) must be solved with the initial condition: $\bar{\boldsymbol{U}}(\bar{s}=0) = \boldsymbol{t}_0$, where $\boldsymbol{t}_0$ is the unit vector tangent to the trajectory at the origin. The whole system is thus governed by only two parameters, namely the initial angle θ_0 and the ratio U_∞/U_0, between the terminal and the initial velocities. In equation (4.5), the last term is initially equal to 1. This value allows us to identify two different regimes:

(i) The parabola

In the low-launching velocity regime ($U_0 \ll U_\infty$), the second term in equation (4.5) is initially much larger than the third and the equation of motion reduces to the classical parabola:

$$\bar{U}\frac{\mathrm{d}\bar{\boldsymbol{U}}}{\mathrm{d}\bar{s}} = -\left(\frac{U_\infty}{U_0}\right)^2 \boldsymbol{e}_y. \tag{4.6}$$

In this regime, the velocity increases from its initial value U_0 to its final value U_∞.

(ii) The Tartaglia curve

In the high-launching speed regime ($U_0 \gg U_\infty$), the second term in equation (4.5) is initially much smaller than the third and the equation of motion reduces to:

$$\bar{U}\frac{\mathrm{d}\bar{\boldsymbol{U}}}{\mathrm{d}\bar{s}} = -\bar{U}\bar{\boldsymbol{U}}, \tag{4.7}$$

which can be integrated as $\bar{\boldsymbol{U}}(\bar{s}) = \boldsymbol{t}_0 \mathrm{e}^{-\bar{s}}$. The initial part of the trajectory is thus a straight line along which the particle decelerates over the characteristic distance $\mathcal{L}$. The final state is also a straight line in which the second and the last term in equation (4.5) compensate: $\boldsymbol{U} = \boldsymbol{U}_\infty$. In between these two regimes, the three terms in equation (4.5) have to be considered in order to connect the two straight lines. These features of the trajectory are very close to the one depicted by Tartaglia and presented in figure 2a. We will thus refer to the trajectories obtained in this large velocity domain as Tartaglias. It is important to underline that in this specific regime the equation of motion never reduces to a parabola. Indeed, the first two terms in equation (4.5) never compensate. These two regimes are illustrated in figure 9 with the low velocity ($U_0/U_\infty = 0.31$) in (a) and the high velocity ($U_0/U_\infty = 100$) in (b).
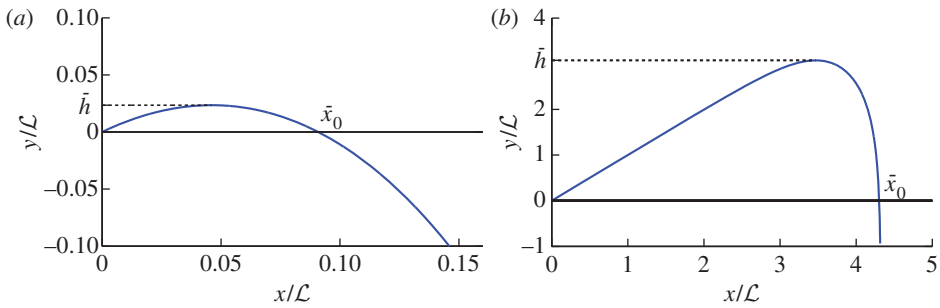
Figure 9. (a,b) Illustration of the two different types of trajectories obtained with the same initial angle $\theta_0 = 45°$: (a) $U_0/U_\infty = 0.31$; (b) $U_0/U_\infty = 100$. (Online version in colour.)
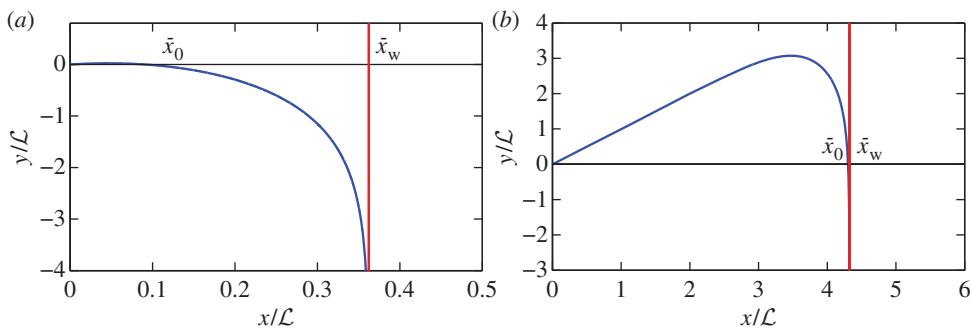

Figure 10. Location of the wall for the two different types of trajectories obtained with the same initial angle $\theta_0 = 45°$: (a) $U_0/U_\infty = 0.31$; (b) $U_0/U_\infty = 100$. (Online version in colour.)

(d) Location of the wall

The aerodynamical wall (or vertical asymptote) is visible in figure 9b but not in figure 9a. To show the existence of the wall in both cases, we zoom out and present in figure 10 the trajectory obtained with the same conditions. We observe that the range $\bar{x}_0$ and the location of the wall $\bar{x}_w$ are distinct in the low-velocity regime (figure 10a), whereas they almost coincide in the high speed limit (figure 10b).

We study analytically the two locations with dimensional quantities. As $\cos \theta = dx/ds$, the location of the wall is defined by $x_w = \int_0^\infty \cos \theta \, ds$. Using $\cos \theta = U_x/U$ and $U_x = U_0 \cos \theta_0 e^{-s/\mathcal{L}}$ (from equation (4.4)), we deduce

$$x_w = U_0 \cos \theta_0 \int_0^\infty \frac{e^{-s/\mathcal{L}}}{U(s)} \, ds. \tag{4.8}$$

To evaluate $U(s)$, we consider separately the two different regimes.

(i) The low-velocity limit: $U_0 \ll U_\infty$

In this regime, the equation of motion initially reduces to $d\mathbf{U}/dt = \mathbf{g}$. Because the velocity is very small at the beginning compared with the terminal velocity, we assume that most of the trajectory which leads to the wall is governed by the equation $U(t) \approx gt$ or $s = 1/2 gt^2$. The equation for wall location (4.8) thus takes the form: $x_w = U_0 \cos \theta_0 \sqrt{2\mathcal{L}/g} \int_0^\infty e^{-\zeta^2} \, d\zeta$, where $\zeta = \sqrt{g/2\mathcal{L}}t$. This
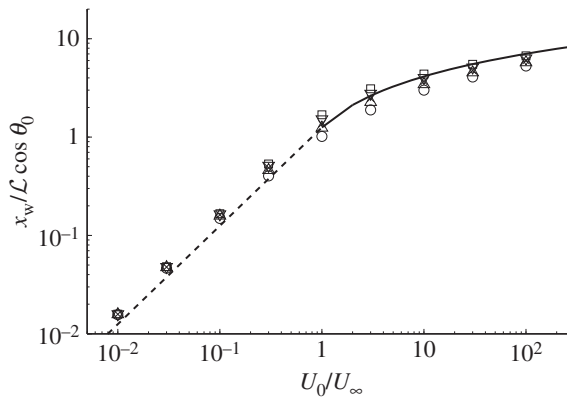
10

rspa.royalsocietypublishing.org Proc. R. Soc. A 470: 20130497

Figure 11. Evolution of the reduced wall location $x_w/\mathcal{L}\cos\theta_0$ as a function of the reduced velocity U_0/U_∞. The symbols have been obtained through the numerical integration of equation (4.5). Each symbol is associated to an initial angle: open triangles, $\theta_0 = 20°$; multiplication symbols, $\theta_0 = 40°$; inverted triangles, $\theta_0 = 60°$, open squares, $\theta_0 = 80°$, open circles, $\theta_0 = -60°$. The solid line represents the analytical solution obtained in the large-velocity regime (4.10). The dashed line presents the analytical solution obtained in the low-velocity domain (4.9).

equation leads to the expression:

$$\frac{x_w}{\mathcal{L}\cos\theta_0} = \sqrt{\frac{\pi}{2}}\frac{U_0}{U_\infty}. \tag{4.9}$$

Equation (4.9) is presented with a dashed line in figure 11. The comparison with the numerical results is fair in the domain $U_0/U_\infty \leq 1$. In this low-velocity regime, the wall location increases linearly with the velocity.

(ii) The large-velocity limit: $U_0 \gg U_\infty$

In this limit, the equation of motion (4.3) initially reduces to $d\boldsymbol{U}/ds = -\boldsymbol{U}/\mathcal{L}$. The velocity thus decreases exponentially over the characteristic distance $\mathcal{L}$: $U(s) = U_0 e^{-s/\mathcal{L}}$. This regime holds up to $s^\star = \mathcal{L}\ln U_0/U_\infty$ where $U(s^\star) = U_\infty$. For larger curvilinear locations, the maximal value of the velocity is the terminal velocity, which leads to the approximation $U(s) = U_\infty$ for $s > s^\star$. In this large velocity regime, the wall location (4.8) thus takes the form: $x_w = \cos\theta_0 \int_0^{s^\star} ds + U_0/U_\infty \cos\theta_0 \int_{s^\star}^\infty e^{-s/\mathcal{L}} ds$ which leads to:

$$\frac{x_w}{\mathcal{L}\cos\theta_0} = 1 + \ln\left(\frac{U_0}{U_\infty}\right). \tag{4.10}$$

This solution is presented with a solid line in figure 11 and compared with the numerical results obtained through the integration of equation (4.5) with different initial conditions. The comparison is satisfactory for velocity ratio larger than unity ($U_0/U_\infty \geq 1$). In this large-velocity regime, the wall location x_w is mainly fixed by the product $\mathcal{L}\cos\theta_0$.

(iii) A composite expression for the wall location

Equations (4.9) and (4.10) can respectively be used in the limits $U_0/U_\infty \ll 1$ and $U_0/U_\infty \gg 1$. The following heuristic equation meets these two limits and holds for all velocities:

$$\frac{x_w}{\mathcal{L}\cos\theta_0} = \left(\frac{(\sqrt{\pi/2}/e)U_\infty/U_0 + U_0/U_\infty}{U_\infty/U_0 + U_0/U_\infty}\right)\ln\left(1 + e \cdot \frac{U_0}{U_\infty}\right) \tag{4.11}$$

(e) An analytical expression for the range

The range, x_0, is defined in figures 3, 7 and 10 as the distance from the origin where the particle returns to its initial height [$y(x_0) = 0$]. This distance differs from 0 only for positive values of θ_0.
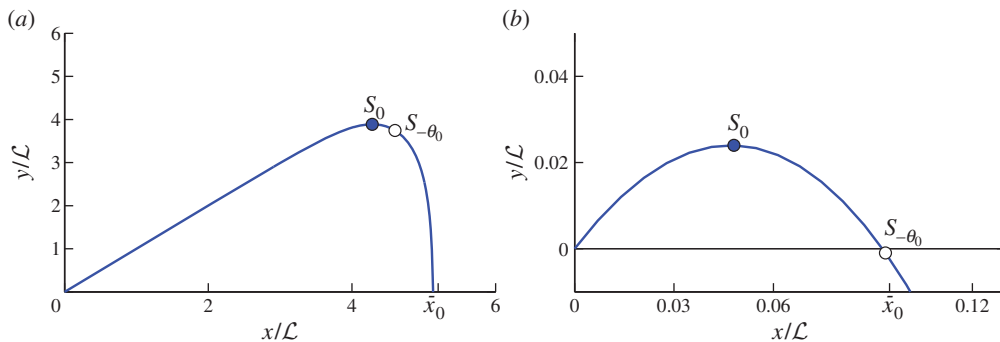
Figure 12. (a) Trajectory obtained from the numerical integration of (4.12) with $\theta_0 = \pi/4$ and $(U_0/U_\infty)^2 = 10^5$. (b) Trajectory obtained from the numerical integration of (4.12) with $\theta_0 = \pi/4$ and $(U_0/U_\infty)^2 = 0.1$. (Online version in colour.)

To obtain the expression of the range in this regime, we use the projection of the equation of motion (4.3) along the direction $\underline{n}$: $U^2 \, d\theta/ds = -g\cos\theta$. Using both the geometrical relation $U^2 = U_x^2/\cos^2\theta$ and equation (4.4) for U_x, we find

$$-\frac{1}{\cos^3\theta}\frac{d\theta}{ds} = \frac{g}{U_{x_0}{}^2}e^{2s/\mathcal{L}}. \tag{4.12}$$

Equation (4.12) can first be integrated numerically and we present in figure 12 the trajectories obtained with $\theta_0 = \pi/4$ and two extreme values of the reduced velocity: $(U_0/U_\infty)^2 = 10^5$ in figure 12a and $(U_0/U_\infty)^2 = 0.1$ in figure 12b. This latter case corresponds to the parabola limit, whereas the first one (strong velocity limit) presents almost a triangular shape. Equation (4.12) can also be integrated by parts which leads to:

$$\left[\ln\left(\frac{1+\sin u}{\cos u}\right) + \frac{\sin u}{\cos^2 u}\right]_\theta^{\theta_0} = \left(\frac{U_\infty}{U_0\cos\theta_0}\right)^2(e^{2s/\mathcal{L}}-1). \tag{4.13}$$

The function $F(u) = \ln((1+\sin u)/\cos u) + \sin u/\cos^2 u$ can be approximated by $G(u) = 2\sin u/\cos^2 u$ (cf. appendix). The integral of trajectory (4.13) relates the local angle θ to the curvilinear coordinate s. In particular, for the maximum ($\theta = 0$), one finds $s_0 = 1/2\mathcal{L}\ln[1 + 2(U_0/U_\infty)^2\sin\theta_0]$. The location of s_0 is presented with a full circle in figure 12. In the triangular shape limit (a), one could use the expression $x_0 \approx s_0\cos\theta_0$ to evaluate the range. However, this evaluation fails by a factor of 2 in the parabolic limit presented in (b). Instead, we use $x_0 \approx s_{-\theta 0}\cos\theta_0$, where $s_{-\theta_0}$ is the curvilinear location at which the local angle gets to the value $\theta(s_{-\theta_0}) = -\theta_0$.

This location is indicated with a white dot in figure 12. This approximation leads to the following expression for the range:

$$x_{0\text{th}} = \frac{1}{2}\mathcal{L}\cos\theta_0\ln\left[1 + 4\left(\frac{U_0}{U_\infty}\right)^2\sin\theta_0\right]. \tag{4.14}$$

At small velocities ($U_0/U_\infty \ll 1$), the logarithmic term can be expanded and equation (4.14) reduces to the classical gravitational result $x_0 = 2U_0^2/g\cos\theta_0\sin\theta_0$. In this domain, the range is very sensitive to the initial velocity ($x_0 \propto U_0^2$). This scaling is different from the one obtained for the wall location, which increases linearly with the velocity. Remarkably, this sensitivity disappears at large velocities: in that limit ($U_0/U_\infty \gg 1$), the logarithmic term weakly increases with the velocity. In that domain, the range is mainly fixed by the product, $\mathcal{L}\cos\theta_0$, which does not depend on the velocity but only on the ball and fluid characteristics.

Analytical expression (4.14) is compared with the numerical results obtained through the integration of equation (4.12) in figure 13. This comparison reveals that the range x_0 is well predicted by equation (4.14) for all initial conditions. The maximum deviation observed in
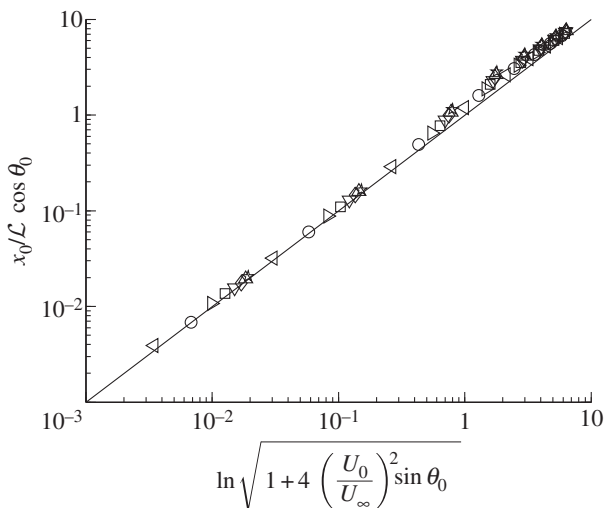
12

rspa.royalsocietypublishing.org *Proc. R. Soc. A* **470**: 20130497

Figure 13. Comparison between the range, x_0, calculated numerically through the integration of equation (4.12) and theoretical expression (4.14). The comparison is performed for different initial velocities and different initial angles: left-pointing triangles, $\theta_0 = 10°$; large circles, $\theta_0 = 20°$; right-pointing triangles, $\theta_0 = 30°$; open squares, $\theta_0 = 40°$; open inverted triangles, $\theta_0 = 50°$; open diamonds, $\theta_0 = 60°$; triangles, $\theta_0 = 70°$; five-pointed open stars, $\theta_0 = 80°$. The solid line represents equation (4.14).

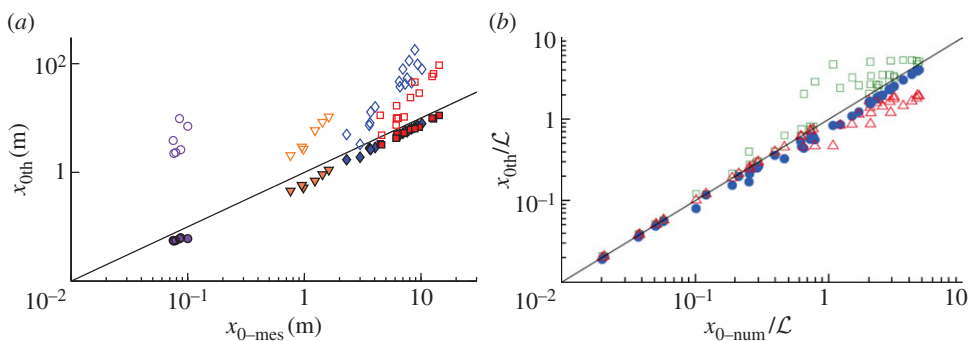**Figure 14.** (*a*) Predicted range $x_{0\text{th}}$ versus measured range $x_{0,\text{mes}}$ for different projectiles (full symbols): filled diamonds, badminton; filled squares, table tennis; inverted filled triangle, balloon; filled circles, underwater sphere. The empty symbols indicate the corresponding parabolic range (no aerodynamic drag) (*b*) Comparison between equation (4.14) presented with (filled circles) and the models of Lamb [9] (open squares) and Chudinov [10] (open triangles). $x_{0\text{th}}/\mathcal{L}$ is the range predicted by each model, $x_{0-\text{num}}/\mathcal{L}$ is the range obtained by numerical integration of the equation of motion. θ_0 varies between 10° and 80° and U_0/U_∞ between 0.1 and 10. In both graphs, the solid line shows the identity. (Online version in colour.)

figure 13 between the range computed numerically and the theoretical expression (4.14) is 25% in the very large velocity limit.

In figure 14*a*, we plot the predicted range $x_{0\text{th}}$ (full symbols) against the measured one $x_{0,\text{mes}}$ for different projectiles (shuttlecock, table tennis ball, balloon and plastic sphere underwater) thrown with various initial speeds and initial angles. The model agrees well with the data. To emphasize the role of the aerodynamic drag, we also plot (empty symbols), the predicted range in the case of no drag (parabolic range). The measurements are much shorter than the parabolic prediction.

We can also compare our work with previous studies. Lamb [9] proposed an approximation of the trajectory $y(x)$, whereas Chudinov gave a different approximation of the range x_0 [10]. For various θ_0 between 10° and 80° and various U_0/U_∞ between 0.1 and 10, we compare in figure 14*b*
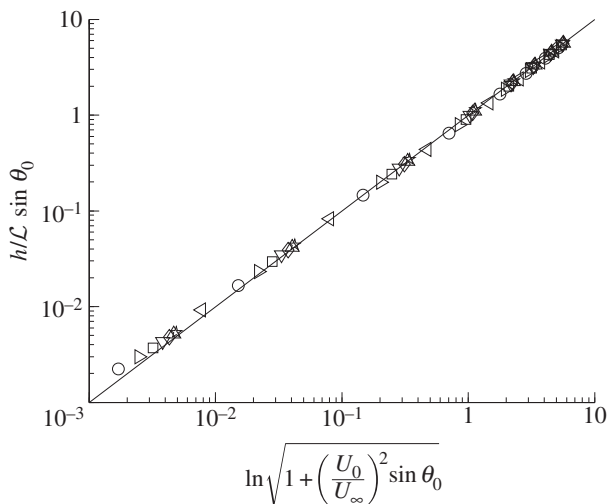
Figure 15. Comparison between the height, h, calculated numerically through the integration of equation (2.2) and the theoretical expression (4.15). The comparison is performed for different initial velocities and different initial angles: left-pointing triangles, $\theta_0 = 10°$; open circles, $\theta_0 = 20°$; right-pointing triangles, $\theta_0 = 30°$; open squares, $\theta_0 = 40°$, inverted triangles, $\theta_0 = 50°$; diamonds, $\theta_0 = 60°$; triangles, $\theta_0 = 70°$; five-pointed open stars, $\theta_0 = 80°$. The solid line represents equation (4.15).

our model with these previous studies. We plot for each model, the predicted range $x_{0th}/\mathcal{L}$ versus the one calculated by integrating numerically the equation of motion $x_{0-num}/\mathcal{L}$. In the parabolic limit ($U_0/U_\infty < 1$), the three models recover the classical values. However, for $U_0/U_\infty > 1$, both previous studies are less accurate than our model.

(f) An analytical expression for the height

To obtain the analytical expression for the height of the trajectory, h, we follow the same steps as for the range: the first integral of the equation of motion (4.13) provides an exact relation between the local angle θ and the curvilinear coordinate s. If we choose the location of the maximum, s_0 ($\theta = 0$), to evaluate the height with the relation $h \approx s_0 \sin \theta_0$, we obtain $h \approx 1/2 \mathcal{L} \sin \theta_0 \ln[1 + 2(U_0/U_\infty)^2 \sin \theta_0]$. In the limit of small velocities, the log term can be expanded and leads to the expression for the height: $h \approx U_0^2/g \sin^2 \theta_0$, which is twice the expected value in this limit.

Instead of $\theta = 0$, we choose an intermediate value θ_1 between θ_0 and 0 such that $\sin \theta_1 / \cos^2 \theta_1 = \sin \theta_0 / \cos^2 \theta_0$. This intermediate value leads to the expression:

$$h_{-th} = \frac{1}{2}\mathcal{L} \sin \theta_0 \ln \left[1 + \left(\frac{U_0}{U_\infty} \right)^2 \sin \theta_0 \right]. \tag{4.15}$$

In the limit of small velocity ($U_0/U_\infty \ll 1$), this expression for the height reduces to the exact value of the parabola. For $\sin \theta_0 = 1$, we also recover the exact solution (4.1) derived in §4a. For different velocities and initial angles, we present in figure 15 the comparison between the height, h, calculated numerically through the integration of equation (4.12) and the theoretical expression (4.15). Over the whole range of initial conditions, the analytical expression of the height (4.15) is in good agreement with the numerical calculation.

(g) The optimal angle $\theta^\star$

Given an initial velocity, the optimal angle $\theta^\star$ is that for which the range is maximized. As the range vanishes for $\theta_0 = 0°$ and $\theta_0 = 90°$, this optimal angle is expected to exist. In the limit of
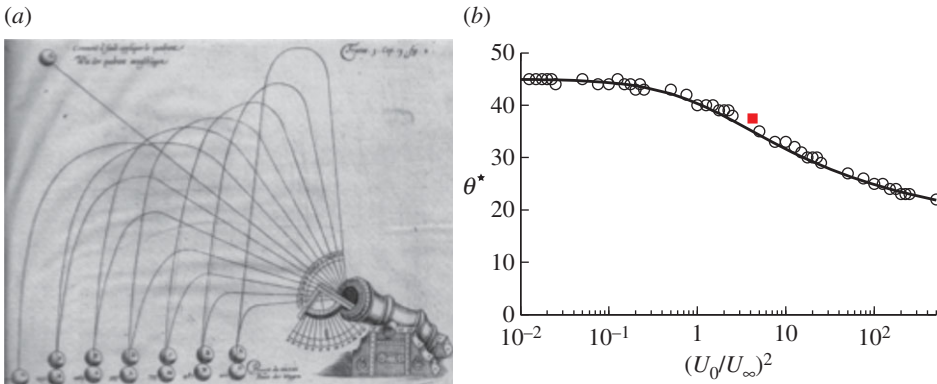
(*a*)

(*b*)

Figure 16. Study of the angle $\theta^\star$ which optimizes the range: (*a*) figure extracted from a treatise in artillery [34]. (*b*) Comparison between the results obtained from the numerical integration of equation (4.12) (big open circles), the analytical expression (4.16) presented with a solid line and the experimental data measured by Hélie (filled squares). (Online version in colour.)

small velocities ($U_0/U_\infty \ll 1$), the parabolic solution leads to $\theta^\star = 45°$. This optimum is known as Tartaglia's law [1] and an illustration is presented in figure 16*a*. Using the numerical integration of equation (4.12), we present in figure 16*b* the evolution of the optimal angle $\theta^\star$ as a function of the reduced velocity $(U_0/U_\infty)^2$. We observe that Tartaglia's law is obeyed in the range $U_0/U_\infty \leq 1$. Above this limit, $\theta^\star$ slowly decreases with increasing velocity: It reaches 30° for $(U_0/U_\infty)^2 = 14$ and 20° for $(U_0/U_\infty)^2 = 1700$.

Because we have an analytical expression for the range (equation (4.14)), the optimal angle can also be determined via the condition $(\partial x_{0th}/\partial \theta_0)_{U_0/U_\infty} = 0$. This condition leads to: $\theta^\star = \arctan \sqrt{X/(1+X)\ln(1+X)}$, where $X = 4(U_0/U_\infty)^2 \cdot \sin\theta^\star$. This implicit equation is difficult to invert. Instead, we use the approximation $X \approx (U_0/U_\infty)^2$ which leads to the expression for $\theta^\star$:

$$\theta^\star = \arctan \sqrt{\frac{(U_0/U_\infty)^2}{[1 + (U_0/U_\infty)^2]\ln[1 + (U_0/U_\infty)^2]}}. \tag{4.16}$$

In the small-velocity limit ($U_0/U_\infty \ll 1$), this expression reduces to $\theta^\star = 45°$. In the large-velocity domain, it leads to $\theta^\star \approx \arctan[1/\sqrt{2\ln(U_0/U_\infty)}]$, which implies a slow decrease in the optimal angle with the velocity. More quantitatively, equation (4.16) is presented in figure 16*b* with a solid line. Over nine decades, it shows a fair agreement with the results obtained numerically through the integration of equation (4.12). For cannonballs, Hélie [35] noted that 'there is an angle which gives the highest range. Experiments show that the angle is always smaller than 45°'. He extracted abacus from experiments performed at Gâvre between 1830 and 1864. For massive cannonballs ($2R = 8$ cm, $M = 15.1$ kg) launched at $U_0 = 485$ m s^{-1}, the large-velocity regime is reached as $U_0/U_\infty = 2.05$. The range is maximized and equal to 5690 m for an angle $\theta^\star = 37.5°$. The solid square reported on figure 16*b* shows that Hélie's data are in agreement with the theoretical and numerical results.

5. Applications and perspectives

(a) Application in fire hoses

Firemen use water guns that produce jets such as those presented in figure 17*a*. The shape of the jet is far from a parabola and exhibits a dissymmetry which appears similar to that of the shuttlecock (figure 5*b*). More quantitatively, we have studied the evolution of the range as a function of the exit velocity using different water guns. The experiments were conducted in the test centre of the company POK S.A. which produces fire equipment. We used a converging water gun similar to
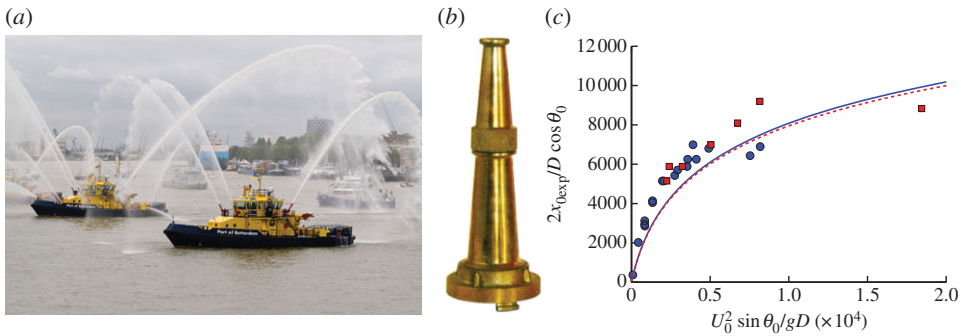
Figure 17. (*a*) Example of jet produced by a water gun (© Gaby Kooijman, http://www.dreamstime.com). (*b*) Typical water gun used in experiments. (*c*) Experimental data showing the evolution of the reduced range, $2x_{0,\mathrm{mes}}/D\cos\theta_0$, of a water gun as a function of the reduced initial velocity $U_0^2\sin\theta_0/gD$. The exit diameter is respectively 6 mm (squares) and 12 mm (circles). The dashed and solid lines are the respective best fits obtained using the analytical expression (4.14) with $\mathcal{L}$ as free parameter. (Online version in colour.)

the one presented in figure 17*b*. The inclination angle was kept constant at $\theta_0 = 30°$ and we used two different exit diameters, $D = 6\,\mathrm{mm}$ (squares) and $D = 12\,\mathrm{mm}$ (circles). The evolution of the reduced range, $2x_0/D\cos\theta_0$, is presented in figure 17*c* as a function of the reduced exit velocity $U_0^2\sin\theta_0/gD$. The two sets of data collapse and exhibit a nonlinear evolution. We have used the analytical expression of the range (4.14) to fit these data: $x_0 = 1/2\mathcal{L}\cos\theta_0\ln[1 + (4U_0^2/g\mathcal{L})\sin\theta_0]$. As $\theta_0 = 30°$ and U_0 is measured, the only free parameter of the fit is $\mathcal{L}$. The fits are presented as continuous lines in figure 17*c*. We find $\mathcal{L} = 20.3\,\mathrm{m}$ and $\mathcal{L} = 40.3\,\mathrm{m}$, respectively, for the diameter 6 and 12 mm. To understand the order of magnitude of this characteristic length scale, one can make a simplified model in which the water gun produces water balls of diameter D. With this model, the characteristic length scale would write $\mathcal{L} = 2M/\rho\pi R_s^2 C_D = 4D\rho_w/3\rho C_D$ (where ρ_w is the water density). Considering measurements of water drops terminal velocities [36], we deduce the value of the drag coefficient associated with those particles: $C_D = 0.44$. This would lead to the value of 18 m for the 6 mm water gun and 36 m for the 12 mm one. So, even if the water jet breaks, it seems that the approximate range of water guns can be predicted by the analytical expression (4.14). A more refined model should consider the break up of the water jet.

(b) Spin effect

If the sphere rotates, it undergoes a side force owing to a Magnus effect. In order to study the modification caused by this effect on the previous study, we observed a soccer ball trajectory in the case of a long clearance. It is known that goalkeepers always put an important backspin in those conditions. Figure 18 reports an example of long clearance recorded from the side of the field.

It is interesting to compare this experimental trajectory with the one expected by solving equation (2.2) numerically with the same initial conditions (dashed line). This resolution includes the experimental value of the aerodynamic length of the soccer ball: $\mathcal{L} = 92\,\mathrm{m}$. The difference between the observed trajectory and that predicted on the basis of our model without spin is significant. The range is about 50% larger experimentally, and the maximal height is doubled. To understand this difference, we need to consider the dynamics of a spinning ball.

In the case of a constant spin $\boldsymbol{\omega}_0$ along the z direction ($\boldsymbol{\omega}_0 = \omega_0\boldsymbol{e}_z$), the trajectory stays in a vertical plane but its shape and range are modified. Taking into account the expression of the side force in the equation of motion, we obtain

$$M\frac{\mathrm{d}\boldsymbol{U}}{\mathrm{d}t} = M\boldsymbol{g} - \frac{1}{2}\rho\pi R^2 C_D U\boldsymbol{U} + \frac{1}{2}\rho\pi R^3 C_R\boldsymbol{\omega}_0 \wedge \boldsymbol{U}. \tag{5.1}$$

16

rspa.royalsocietypublishing.org *Proc. R. Soc. A* **470**: 20130497
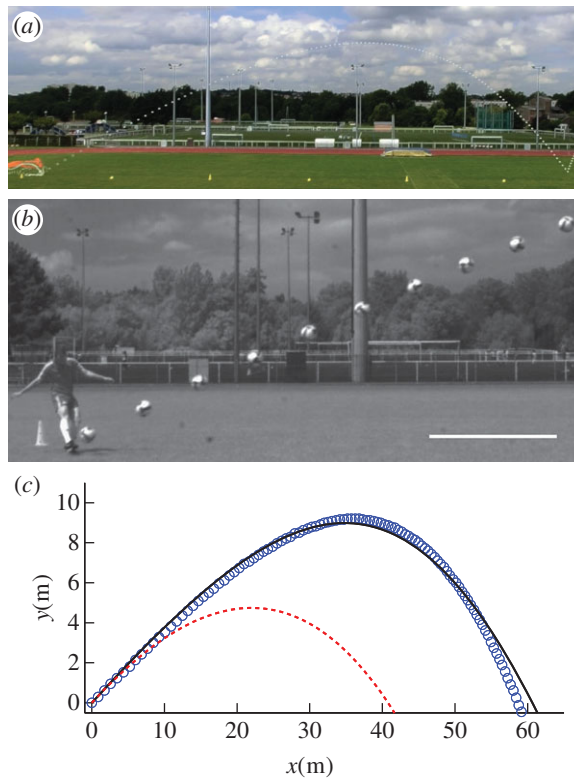...

Figure 18. (*a*) Chronophotography of a soccer ball long clearance viewed from the side of the field. Each ball position is separated by 33 ms and the pads on the ground are separated by 10 m (the total width is thus of the order of 60 m). (*b*) Zoom on the first part of the chronophotography. The scale bar indicates 2 m. The timestep is 40 ms. (*c*) Trajectories of long clearance. Open circles correspond to the experimental trajectory viewed from the side of the field. The dotted line stands for the trajectory with same initial conditions but without spin. The latter is obtained by solving numerically equation (2.2) with the experimental value of the aerodynamic length: $\mathcal{L} = 92$ m. The solid black line represents the solution of equations (5.2) and (5.3) taking into account the initial spin of the ball and considering $\mathcal{L}/\mathcal{L}_R = 2.3$. (Online version in colour.)

Along the t and n directions (cf. figure 3), the previous equation can be written in a non-dimensional way with $\bar{s} = s/\mathcal{L}$, $\bar{U} = U/U_0$ and $\bar{t} = tU_0/\mathcal{L}$. This provides the two following equations:

$$\frac{\mathrm{d}\bar{U}}{\mathrm{d}\bar{t}} = -\left(\frac{U_\infty}{U_0}\right)^2 \sin\theta - \bar{U}^2 \tag{5.2}$$

and

$$\frac{\mathrm{d}\theta}{\mathrm{d}\bar{t}} = -\left(\frac{U_\infty}{U_0}\right)^2 \frac{\cos\theta}{\bar{U}} + \frac{\mathcal{L}}{\mathcal{L}_R}\frac{R\omega_0}{U_0}, \tag{5.3}$$

where $\mathcal{L}_R = 2M/\rho\pi R^2 C_R$ is a typical distance over which the spin curves the trajectory. The two non-dimensional parameters which characterize the effect of ball rotation on the trajectory are $\mathcal{L}/\mathcal{L}_R$ and $Sp_0 = R\omega_0/U_0$. This latter parameter, also called 'spin number', compares the rotation and translation speeds. Sp_0 depends on the initial launching conditions whereas $\mathcal{L}/\mathcal{L}_R$ only depends on ball and fluid properties. We solve numerically equations (5.2) and (5.3) with the initial conditions of the experimental soccer long clearance. This calculation is performed with $\mathcal{L} = 92$ m, the experimental value of the initial ball spin ω_0 and considering $\mathcal{L}/\mathcal{L}_R$ as an adjustable parameter. We find that $\mathcal{L}/\mathcal{L}_R = 2.3$ is the value which minimizes the error between ten different experimental trajectories and numerical ones. In the case of the clearance shown in figure 18, this approach provides the numerical trajectory drawn with a solid black line. The agreement
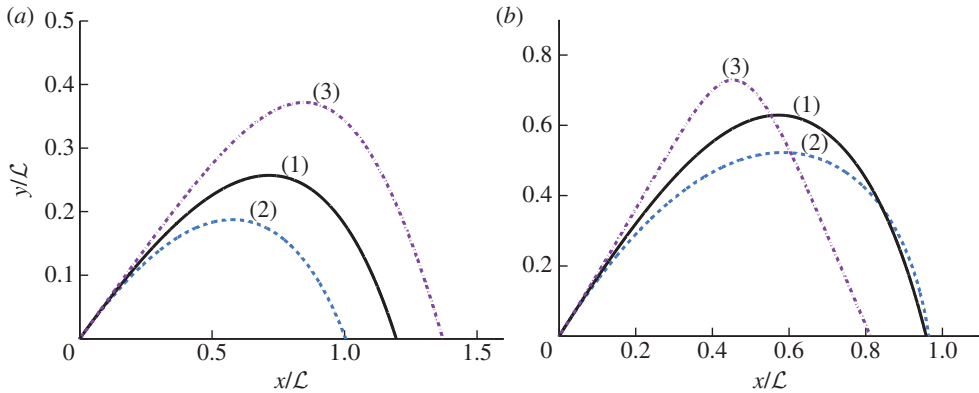
Figure 19. Example of trajectories with no spin (1), top spin ($Sp_0 = -0.1$ in (2)) and back spin ($Sp_0 = +0.1$ in (3)) for the same initial angle and velocity. Initial conditions are (a) $\theta_0 = 30°$ and $U_0/U_\infty = 1$, (b) $\theta_0 = 60°$ and $U_0/U_\infty = 1$. The ratio $\mathcal{L}/\mathcal{L}_\mathcal{R}$ is assumed to be constant and equal to 2.3. (Online version in colour.)
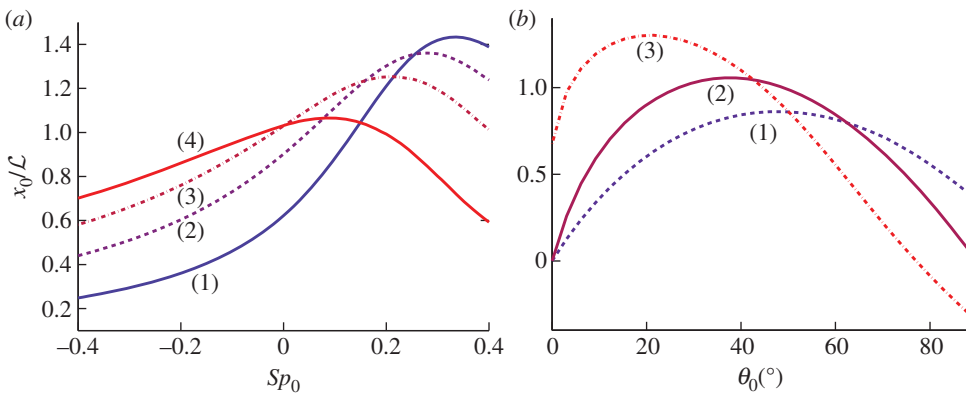

Figure 20. Numerical study of the effect of the spin on the range for $U_0/U_\infty = 1.7$ and $\mathcal{L}/\mathcal{L}_R = 2.3$: (a) effect of the spin number on the reduced range $x_0/\mathcal{L}$ for different values of θ_0: 10° (1), 20° (2), 30° (3) and 45° (4). (b) Effect of the launching angle θ_0 on the reduced range $x_0/\mathcal{L}$ for different values of spin number Sp_0: -0.2 (1), 0 (2) and $+0.2$ (3). (Online version in colour.)

between this trajectory and the experimental one validates our assumptions, that is to say a constant rotation rate and no dependency of C_R with Sp and Re. The first assumption is driven by the fact that the spin rate decreases on a longer timescale than the translation velocity [37]. The second assumption is consistent with the conclusions drawn by Nathan for baseballs in the range of spin number and Reynolds number experienced during the game [26]. Moreover, from $\mathcal{L}/\mathcal{L}_R = 2.3$ we deduce $C_R = 0.52$ which is in the range of values determined by Nathan for baseballs ($C_R \simeq 0.5 \pm 0.1$).

Solving equations (5.2) and (5.3) numerically allows us to evaluate the modified range x_0 for a wide range of initial conditions and parameters. Typical examples of numerical solutions are reported in figure 19.

Quantitatively, the effect of the spin and initial launching angle on the range is shown in figure 20. The numerical study is conducted with $U_0/U_\infty = 1.7$ and $\mathcal{L}/\mathcal{L}_\mathcal{R} = 2.3$ (soccer conditions).

Focusing on figure 20a, we observe a non-monotonic evolution of the range with the spin number. The optimum value depends on the launching angle. The smaller the angle, the larger the range at the optimum and the larger the spin.
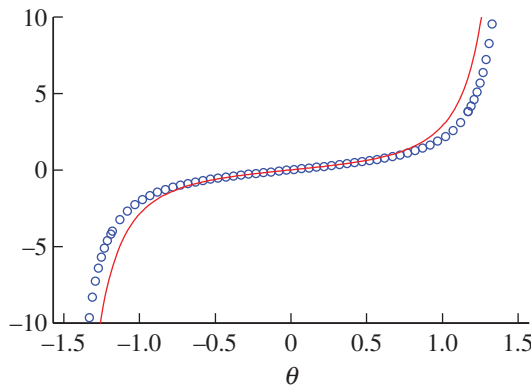
18

rspa.royalsocietypublishing.org   *Proc. R. Soc. A* **470**: 20130497

Figure 21. Functions $F(u)$ (solid line) and its approximation $G(u)$ (open circles). (Online version in colour.)

For a given spin number, the evolution of the range with the launching angle is shown in figure 20b. Again, the evolution presents an optimum, the value of which increases with the spin number. The larger the backspin effect, the larger the range at the maximum and the smaller the optimal launching angle. For example, with $Sp_0 = +0.2$, the maximal range is $x_0/\mathcal{L} \approx 1.4$ and is obtained with $\theta_0 = 20°$. With such a backspin, the goal keeper thus increases the range of his clearance by 40% compared with the non-spinning limit.

6. Conclusion

The trajectories of particles under the influence of gravity and drag at large Reynolds numbers are studied. Each particle is characterized by its terminal velocity for which the drag balances the weight. We show that depending on the launching speed, two different types of trajectories can be observed: when the initial velocity is smaller than the terminal one, the particle describes the classical Galilean parabola. However, when the launching speed exceeds the terminal velocity the trajectory is never a parabola but an asymmetric curve that we have called a Tartaglia. In both limits, the trajectory exhibits a vertical asymptote (aerodynamical wall) for which we have provided an analytical expression. Apart from the wall location, we also study the range and the height. These three quantities exhibit a logarithmic saturation at large velocities. This saturation has implications in several domains and we have discussed more precisely its influence in the determination of water hose performance and how spin can make a difference in the flight of sports balls.

Appendix A: function $F(\theta)$

The theoretical development of the equation of the motion leads to the function $F(\theta)$ defined on the interval $I =] - \pi/2; \pi/2[$:

$$F(\theta) = \int \frac{d\theta}{\cos^3 \theta} = \frac{1}{2} \left[\frac{\sin \theta}{\cos^2 \theta} + \ln \left(\frac{1 + \sin \theta}{\cos \theta} \right) \right]. \tag{A 1}$$

We introduce $G(\theta) = \sin\theta / \cos^2\theta$ and $H(\theta) = \ln[(1 + \sin\theta) / \cos\theta]$, so that $F = 1/2[G(\theta) + H(\theta)]$. Studying those two functions, we see that for $\theta \to 0$, $G \sim H$, and for $\theta \to \pm\pi/2$, G and H diverge with $|G| \gg |H|$. We thus approximate $F(\theta)$ by $G(\theta)$:

$$F(\theta) \approx \frac{\sin\theta}{\cos^2\theta}. \tag{A 2}$$

Figure 21 shows the functions F and G. We see that the approximation of F by G is quite good.

References

1. Tartaglia N. 1537 *Nova scienta*. Venice, Italy: A. Forni Editore, 1984.
2. Galilei G. 1638 *Dialogues concerning two new sciences*. New York, NY: Dover.
3. Drake S. 1973 Galileo's experimental confirmation of horizontal inertia: unpublished manuscripts. *Isis* **64**, 291–305. (doi:10.1086/351124)
4. Tartaglia N. 1846 *La balistique*. Correard, Editeur d'ouvrages militaires.
5. Charbonnier P. 1904 *Traité de balistique extérieure*. Paris, France: Librairie Polytechnique.
6. Mehta R. 1985 Aerodynamics of sports balls. *Annu. Rev. Fluid Mech.* **17**, 151–189. (doi:10.1146/annurev.fl.17.010185.001055)
7. Euler L. 1755 Recherches sur la veritable courbe que decrivent les corps jettes dans l'air ou dans un autre fluide quelconque. *Mem. Aad. Sci. Berlin* **9**, 321–352.
8. De Mestre N. 1990 *The mathematics of projectiles in sport*. New York, NY: Cambridge University Press.
9. Lamb H. 1914 *Dynamics*. Cambridge, UK: Cambridge University Press.
10. Chudinov PS. 2001 The motion of a point mass in a medium with a square law of drag. *J. Appl. Maths Mech.* **65**, 421–426. (doi:10.1016/S0021-8928(01)00047-8)
11. Darrigol O. 2005 *Worlds of flow*. Oxford, UK: Oxford University Press.
12. Stokes GG. 1851 On the effect of internal friction of fluids on the motion of pendulums. *Trans. Camb. Philos. Soc.* **9**, 8–106.
13. Davies CN. 1945 Definitive equations for the fluid resistance of spheres. *Proc. Phys. Soc. Lond.* **57**, 259–270. (doi:10.1088/0959-5309/57/4/301)
14. Pruppacher HR. 1968 An experimental determination of the drag on a sphere at low Reynolds numbers. *J. Appl. Phys.* **39**, 4129–4132. (doi:10.1063/1.1656936)
15. Batchelor GK. 1967 *An introduction to fluid dynamics*. Cambridge, UK: Cambridge University Press.
16. Newton I. 1686 *Philosophae naturalis principia mathematica*. London, UK: S. Pepys Reg. Soc. Praeses.
17. Eiffel G. 1909 *Recherches expérimentales sur la résistance de l'air exécutées à la tour Eiffel*. Paris, France: Librarie aéronautique, Editions Chiron, 1919.
18. Oseen CW. 1910 Ueber die stokes'sche formel, und iiber eine venvandt.e aufgabe in der hydrodynamik. *Ark. Math. Astronom. Fys.* 6.
19. Benjamin TB. 1993 Note on formulas for the drag of a sphere. *J. Fluid Mech.* **246**, 335–342. (doi:10.1017/S0022112093000151)
20. Lyotard N, Shew WL, Bocquet L, Pinton J-F. 2007 Polymer and surface roughness effects on the drag crisis for falling spheres. *Eur. Phys. J. B* **60**, 469–476. (doi:10.1140/epjb/e2008-00018-0)
21. Smith MR, Hilton DK, Van Sciver SW. 1999 Observed drag crisis on a sphere in flowing He I and He II. *Phys. Fluids* **11**, 751–753. (doi:10.1063/1.869947)
22. Achenbach E. 1972 Experiments on the flow past spheres at very high Reynolds numbers. *J. Fluid Mech.* **54**, 565–575. (doi:10.1017/S0022112072000874)
23. Barkla HM, Auchterloniet LJ. 1971 The magnus or robins effect on rotating spheres. *J. Fluid Mech.* **47**, 437–447. (doi:10.1017/S0022112071001150)
24. Robins B. 1805 *New principles of gunnery* (ed. Hutton) (first printed in 1742). Richmond, UK: Richmond Publishing Co. Ltd. 1972.
25. Magnus G. 1853 Ueber die abweichung der geschosse, und eke auffallende erscheinung bei rotirenden korpern. *Poggendorfs Annalen der Physik urui Chemie* **88**, 1.
26. Nathan AM. 2008 The effect of spin on the flight of a baseball. *Am. J. Phys.* **76**, 119–124. (doi:10.1119/1.2805242)
27. Davies JM. 1949 The aerodynamics of golf balls. *J. Appl. Phys.* **20**, 821–828. (doi:10.1063/1.1698540)

28. Bush JW. 2013 The aerodynamics of the beautiful game. In *Sport physics*. Palaiseau, France: Editions de l'Ecole Polytechnique.

29. Mehta RD, Pallis JM. 2001 Sports ball aerodynamics: effects of velocity, spin and surface roughness. *Minerals, Metals Mater. Soc./AIME, Mater. Sci. Sports* (*USA*) 185–197.

30. World-Directory. 1990 *World directory of aerospace vehicle research and development*. Washington, DC: World-Directory.

31. Haynes MW (ed.) 2013 *CRC handbook of chemistry and physics*, vol. 93. New York, NY: CRC.

32. Schlichting H. 1955 *Boundary-layer theory*. New York, NY: McGraw Hill.

33. Cooke AJ. 1999 Shuttlecock aerodynamics. *Sport Eng.* **2**, 85–96. (doi:10.1046/j.1460-2687.1999.00023.x)

34. Ufano D. 1628 *Artillerie ou vraye instruction de l'artillerie et de ses appartenances*. Rouen, France: Jean Berthelin.

35. Félix Hélie. 1884 *Traité de balistique expérimentale*, vol. 1. Paris, France: Gauthier-Villars.

36. Beard KcV, Pruppacher HR. 1969 A determination of the terminal velocity and drag of small water drops by means of a wind tunnel. *J. Atmos. Sci.* **26**, 1066–1072. (doi:10.1175/1520-0469(1969)026<1066:ADOTTV>2.0.CO;2)

37. Dupeux G, Le Goff A, Quéré D, Clanet C. 2010 The spinning ball spiral. *N. J. Phys.* **12**, 093004. (doi:10.1088/1367-2630/12/9/093004)

20

rspa.royalsocietypublishing.org *Proc. R. Soc. A* **470**: 20130497